


# Origin of Two Distinct Stress Relaxation Regimes in Shear Jammed Dense Suspensions

Sachidananda Barik and Sayantan Majumdar<sup>\*</sup>*Soft Condensed Matter Group, Raman Research Institute, Bangalore 560080, Karnataka, India*
 (Received 1 October 2021; revised 5 May 2022; accepted 8 June 2022; published 23 June 2022)

Many dense particulate suspensions show a stress induced transformation from a liquidlike state to a solidlike shear jammed (SJ) state. However, the underlying particle-scale dynamics leading to such striking, reversible transition of the bulk remains unknown. Here, we study transient stress relaxation behaviour of SJ states formed by a well-characterized dense suspension under a step strain perturbation. We observe a strongly nonexponential relaxation that develops a sharp discontinuous stress drop at short time for high enough peak-stress values. High resolution boundary imaging and normal stress measurements confirm that such stress discontinuity originates from the localized plastic events, whereas system spanning dilation controls the slower relaxation process. We also find an intriguing correlation between the nature of transient relaxation and the steady-state shear jamming phase diagram obtained from the Wyart-Cates model.

DOI: [10.1103/PhysRevLett.128.258002](https://doi.org/10.1103/PhysRevLett.128.258002)

Stress induced enhancement of viscosity in dense particulate suspensions, commonly known as shear-thickening [1–4], has attracted significant recent interest both from the fundamental point of view and material design [5–11]. For high enough particle volume fraction and applied stress, many of these systems show a remarkable transition to a shear jammed (SJ) state showing stress-activated solidlike yield stress [12–14]. Although the phenomenon of shear-thickening has been well-known for the past few decades, the difference between the SJ state and strong or discontinuous shear-thickened (DST) state has been demonstrated only recently and remains a topic of intense research [12,15–18]. SJ results from the stress induced constraints on sliding and rolling degrees of freedom of particles [15,16,19]. Such constraints can originate from frictional, hydrodynamic, and other short-range interparticle interactions [15,17,20]. For a steady-state flow of frictional systems, the Wyart-Cates (W-C) model provides microscopic insight into the stress ( $\sigma$ ) induced increase in viscosity in terms of a single order parameter  $f = f(\sigma)$ : the fraction of frictional contacts in the system [6]. A recent continuum model [21] that treats the parameter  $f$  as a spatially varying field with specific time evolution can quantitatively describe a range of striking flow behaviors in these systems. Once the applied perturbation is removed, the SJ state quickly relaxes back to the unperturbed fluidlike state. Such fast reversibility coupled with the high stress bearing ability of SJ systems [4], remain at the heart of many potential applications.

The nature of relaxation in dense suspensions close to jamming is complex and is sparsely explored in the context of systems showing DST and SJ: Above a critical deformation rate, dense suspensions of PMMA nanoparticles show two distinct relaxation processes [22]; in dense

cornstarch suspensions the relaxation behavior deviates significantly from a generalized Newtonian model [23], and many aspects of the relaxation can be captured by a continuum theoretical model [21,24]. In dense polystyrene ethyl acrylate nanoparticle suspensions, a multielement viscoelastic model consistent with the expected force chain structure fits the relaxation behavior well [25]. Two-step relaxation has also been observed in glassy and static-jammed materials [26,27]. However, the extremely slow nature of relaxation and the existence of residual stresses in these systems highlight the widely different underlying microscopic dynamics as compared with the dense suspensions showing DST and SJ.

Despite these detailed studies, the role of microscopic particle-scale dynamics in controlling the bulk relaxation of the SJ state is not understood. Importantly, due to its solidlike nature, a sustained steady-state flow is not possible in SJ systems [18]. Thus, in earlier studies the mechanical state of the SJ sample just prior to relaxation remains poorly characterized. Recent experiments suggest that the mechanical properties of SJ states can be probed reliably under transient perturbations [12,13,17,28]. Numerical simulations probing transient relaxation in overdamped, athermal dense suspensions of frictionless spheres found a power-law cutoff by an exponential relaxation close to the isotropic jamming point ( $\phi_0$ ) with the relaxation time diverging at  $\phi = \phi_0$  [29,30]. However, the relevance of such findings for SJ systems remains unclear due to the difference in stress dependence of the constraints in frictionless and frictional systems [16].

In this Letter, we address these issues by studying the transient stress relaxation behavior of SJ states in dense suspensions of colloidal polystyrene particles (PS) dispersed in polyethylene glycol (PEG) using shear rheology

in conjugation with high resolution boundary imaging. We observe a power-law cutoff by a stretched-exponential relaxation for moderate stress values; however, a sharp discontinuous relaxation after the power-law regime is observed for large stresses. We directly correlate, for the first time, plasticity and dilation in the system with the timescales associated with the bulk relaxation dynamics. We also uncover an interesting connection between the transient relaxation phenomena and the steady-state SJ (SSSJ) phase diagram obtained using the W-C model.

The shear thickening dense suspensions are prepared by dispersing monodisperse PS (diameter =  $2.65 \pm 0.13 \mu\text{m}$ ) in PEG [18] for a range of volume fractions. See Supplemental Material [31] for details, which also includes Refs. [32–38]. As a transient perturbation, a step shear strain of a certain magnitude ( $\gamma$ ) is applied to the sample for 25 s. We record the resulting stress response. Due to instrumental limitation the applied strain reaches the set value after a time  $t_0 \approx 0.06$  s as shown in Fig. 1(a). Shear stress in the system quickly reaches a maximum ( $\sigma_p$ ) and then starts to relax. We find that the nature of stress relaxation is determined by the magnitude of  $\sigma_p$  that depends on both  $\phi$  and  $\gamma$ . We observe that for  $57\% \leq \phi \leq 61\%$  ( $\phi$  range corresponds to SSSJ; see Fig. S1 in the Supplemental Material [31]), the stress relaxation is given by  $\sigma(t) \sim t^{-\alpha} e^{-(t/\tau)^\beta}$  for values of  $\sigma_p$  up to  $\sim 16$  kPa.

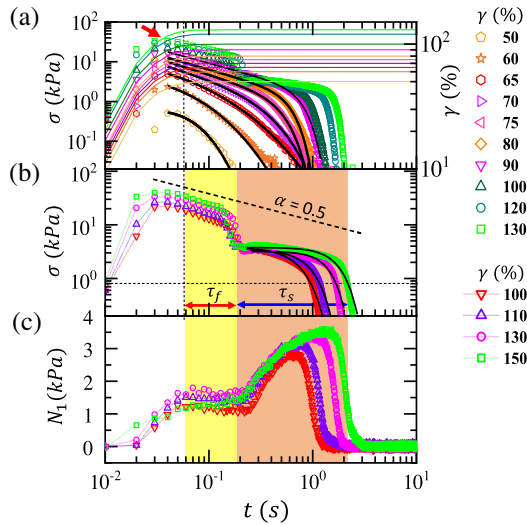


FIG. 1. (a) Shear stress  $\sigma$  as a function of time  $t$  (symbols) under different applied step strains  $\gamma$  (thin lines). Solid lines are the fits to the power-law cutoff by a stretched exponential function (main text). The arrow indicates peak stress ( $\sigma_p$ ) for  $\gamma = 130\%$ . (b) Plots of  $\sigma$  vs  $t$  for  $\gamma \geq 100\%$  showing a self similarity. Power-law decay with slope 0.5 is also indicated. Solid lines show typical stretched exponential fits after the discontinuous stress drop. The fast  $\tau_f$  (yellow shade) and slow  $\tau_s$  (brown shade) relaxation timescales are marked. (c) Evolution of first normal stress difference  $N_1$  corresponding to the data shown in panel (b). In all cases  $\phi = 58\%$  and solvent viscosity  $\eta_l = 80$  mPa.s.

Remarkably, for  $\sigma_p > 16$  kPa, we find a discontinuous stress drop soon after the power-law decay regime by almost 1 order of magnitude [Figs. 1(a) and 1(b)]. After this, the stretched exponential function still captures the long-time relaxation fairly well. Similar trends are also observed for other  $\phi$  values in the SSSJ regime, but the magnitude of the discontinuous stress drop increases for larger  $\phi$  values [Figs. S2(a) and S2(b) in the Supplemental Material [31]]. In all cases, the magnitude of the power-law exponent ( $\alpha$ ) decreases with increasing  $\sigma_p$  and finally saturates at  $\alpha \approx 0.5$  except for  $\phi = 57\%$ , where we get a higher saturation value [Fig. S3(a) in the Supplemental Material [31]]. Just below SJ ( $\phi < 57\%$ ), the power-law regime disappears, and a stretched exponential relaxation is observed for a wide range of  $\sigma_p$  [Fig. S3(b) in the Supplemental Material [31]]. Interestingly, we observe similar relaxation dynamics for a variety of dense suspensions showing SJ [Fig. S3(c) in the Supplemental Material [31]] indicating a universal behavior. For quantification, we define two timescales for such discontinuous stress relaxation: a fast timescale  $\tau_f$  (after  $t_0$ ) at which the discontinuous stress drop takes place and a slower one  $\tau_s$  indicating the time (after  $\tau_f$ ) for the stress to drop to  $\sigma_d = 0.05\Gamma/a$  [39] ( $\Gamma$ : surface tension of solvent-air interface,  $a$ : particle diameter). Notably, most of the stress in the system relaxes within  $t = \tau_f$ . In Fig. 1(c), we show the variation of the first normal stress difference  $N_1 = (2F_N/\pi r^2)$  (for cone-plate geometry where  $F_N$  is the normal force on the plate or cone) corresponding to the stress relaxation data shown in Fig. 1(b). In all cases we find that  $N_1$  shows a clear positive peak at a longer time near  $\sigma = \sigma_d$ , with the instantaneous shear stress  $\sigma(t) \approx N_1$  near the peak. On the other hand, the behavior of  $N_1$  remains arbitrary [Fig. 1(c) and also Figs. S2(a) and S2(b) in the Supplemental Material [31]] for  $t < \tau_f$  and  $\sigma(t) \gg N_1$  in this regime. Such interesting decoupling of the shear and the normal stress response is not observed for SSSJ (Fig. S1 in the Supplemental Material [31]) [40]. For smaller  $\sigma_p$  values (smooth relaxation regime) we find that the magnitude of the peak in  $N_1$  monotonically decreases with decreasing  $\sigma_p$ . Also, the peak gradually shifts toward the smaller timescales and completely disappears for sufficiently small values of  $\sigma_p$  (Fig. S4 in the Supplemental Material [31]).

To correlate the complex relaxation process with the particle-scale dynamics, we use high-resolution *in situ* optical imaging of the sample boundary in the flow-gradient plane [41]. For sufficiently high  $\sigma_p$ , we see an enhanced brightness of the sample boundary across the entire shear gap (Movie, S1 in the Supplemental Material [31]) due to dilation [39]. The boundary intensity returns back to the initial unperturbed value once the shear stress relaxes below  $\sigma_d$ . Surprisingly, for high  $\sigma_p$  values, where the stress relaxation becomes discontinuous (beyond a critical

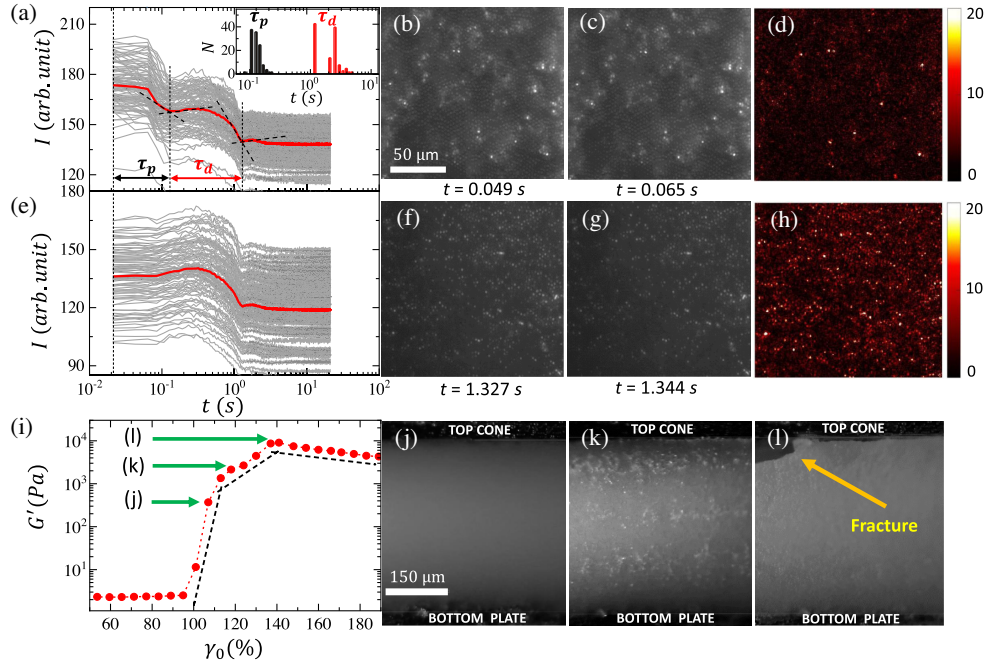


FIG. 2. Intensity  $I$  as a function of time  $t$  (gray lines) for different regions with (a) and without (e) PCs with the average behaviors (thick red lines) are also indicated. Here, the starting time for each graph corresponds to an absolute time  $t = t_0$  as mentioned in Fig. 1. Relaxation time for PC ( $\tau_p$ ) and dilation ( $\tau_d$ ) are marked with vertical dash lines in (a). Inset: distribution of  $\tau_p$  and  $\tau_d$  ( $N = 130$ ). (b) and (c) Consecutive images of the sample boundary, during the fast relaxation, and the corresponding difference image is shown in (d). (f) and (g) Consecutive images of the sample boundary, during slow relaxation, and the corresponding difference image shown in (h). (i) Elastic modulus ( $G'$ ) vs strain amplitude ( $\gamma_0$ ). Dashed lines represent the slope in different  $\gamma_0$  regimes with the corresponding boundary images shown in panels (j), (k), and (l).  $\phi = 61\%$  and  $\eta_l = 80$  mPa.s in all cases.

magnitude of  $\gamma$ ), we find randomly distributed bright spots (width: 1–2 particle diameter) [Figs. 2(b) and 2(c); also, Movie in S1 and S2 of the Supplemental Material [31]] on the sample boundary. At high enough  $\sigma_p$  these bright spots can combine to create a macroscopic fracture in the sample (Fig. S5 in the Supplemental Material [31]). Using oscillatory rheology, we find that the appearance of these bright spots is correlated with the onset of weakening or plasticity of the SJ state, as marked by the decrease in slope of  $G'$  vs  $\gamma_0$  [Figs. 2(i)–2(l) and Fig. S6 in the Supplemental Material [31]]. This implies that these spots indicate localized plasticity or microfracture over the particle length scales, and we term them as *plastic centers* (PCs). We find that the number of such PCs increases with  $\gamma$  before a fracture appears (Fig. S7 in the Supplemental Material [31]). During stress relaxation, we find that PCs disappear quickly before a gradual decrease of surface intensity takes place. To quantify the time dependence of intensity relaxation we plot the variation of average intensity  $I(t)$  as a function of time over a small region ( $\sim 13.6 \mu\text{m}^2$ ) around each PC [Fig. 2(a)], as well as similar regions that do not contain any PC [Fig. 2(e)]. For both of these regions, the intensity relaxation remains self-similar as indicated by the mean curves in Figs. 2(a) and 2(e). For PCs we observe that  $I(t)$  shows a two step relaxation similar to  $\sigma(t)$ . Due to the small dynamic range of intensity relaxation, we define the associated timescales from

the crossover points [Fig. 2(a)]. We denote the fast timescale as  $\tau_p$  and the slower one as  $\tau_d$ . For regions without PCs, we find that the short-time drop in intensity is missing, but the slower relaxation behavior is very similar to that obtained for PCs. Interestingly, we find that the values of  $\tau_p$  and  $\tau_d$  are distributed with peaks around  $t \approx 0.2$  s and 2 s, respectively [inset of Fig. 2(a)] showing a strong correlation with the stress relaxation timescales  $\tau_f$  and  $\tau_s$ . This implies that the rapid stress relaxation of the SJ state is related to the dynamics of PC, whereas the slower relaxation is governed by the dilation dynamics. Nonetheless, dilation is also present during the PC relaxation due to high stress in the system. During the PC relaxation, there is stress injection in the system due to fluidization of local jammed regions. This is reflected in the sudden rearrangement and slight enhancement of the surface intensity indicating a stronger dilation beyond  $t = \tau_p$  [Fig. 2(e) and also Movie, S2 in the Supplemental Material [31]]. This results in the peak in  $N_1$  [around  $t = 1$  s in Fig. 1(c)]. Such dynamic local jammed regions have also been observed in recent simulations [42]. To get a deeper insight into this striking intensity relaxation dynamics, we calculate the intensity difference between two consecutive images  $\Delta I = |I(x, y, t) - I(x, y, t + \Delta t)|$  ( $\Delta t = 0.016$  s) during both PC [Figs. 2(b) and 2(c)] and dilation [Figs. 2(f) and 2(g)] relaxation. The appearance of a bright spot in  $\Delta I$  at a particular spatial position indicates a

local particle rearrangement at that position over a time  $\Delta t$ . We find that during PC relaxation  $\Delta I$  shows only a few isolated bright spots [Fig. 2(d)], whereas, during dilation relaxation, we obtain a large number of bright spots uniformly distributed throughout the field of view [Fig. 2(h)]. This indicates that PC relaxation is governed by abrupt localized rearrangements, whereas dilation relaxation happens by more gradual rearrangements throughout the system. We conjecture that since the PCs are sensitive to only local constrains, PC relaxation is much faster compared with dilation relaxation involving global constrains. Such a picture physically predicts the origin of the temporally distinct stress relaxation regimes. We do not observe any significant change in average particle distribution before and after the PC relaxation (Fig. S8 in the Supplemental Material [31]), further confirming the spatially localized nature of PC relaxation. In our system, the interparticle contact formation timescale  $\eta_l \gamma / \sigma^* \sim 4 \times 10^{-4}$  s ( $\sigma^*$ : onset stress for contact formation) is negligible compared with the relaxation timescales, implying that the relaxation is governed by the relaxation dynamics of contact networks [24,43]. Importantly, such contact networks not only get stronger with increasing applied stress, but beyond a critical value significant stress induced reorganizations can happen through the buckling and eventual breaking of the force chains [21,44] close to jamming. For rigid particle systems such buckling can take place even at moderate stress values due to the small area of contact (see the Supplemental Material [31]). We also correlate the local plastic rearrangements with the discontinuous stress relaxation. We find an enhancement of the number of such rearrangements at the point of sharp stress drop (Fig. S9 in the Supplemental Material [31]). Such correspondence has also been observed in the context of granular plasticity [45,46]. In dry granular systems, x-ray tomography reveals that equivalent to nearest neighbor exchange ( $T1$  events) in 2D, particle-pair exchange neighbors resulting in defects of poly-tetrahedral order in 3D [47]. However, we do not observe any  $T1$  event from our 2D imaging.

To test our conjecture regarding the fast and slow timescales, we probe the effect of solvent viscosity ( $\eta_l$ ) and particle volume fraction ( $\phi$ ) on the stress or intensity relaxation timescales. We see from Fig. 3(a) that the average value of fast timescales obtained from the stress relaxation ( $\tau_f$ ) and boundary imaging ( $\tau_p$ ) remain almost independent of  $\phi$ . However, the slow timescales  $\tau_s$  and  $\tau_d$  show an increasing trend with the increase in  $\phi$  before saturating for  $\phi \geq 59\%$ . A similar trend is also observed for the change in solvent viscosity [Fig. 3(a), inset]:  $\tau_f$  remains independent of  $\eta_l$ , but  $\tau_s$  increases with the increase in  $\eta_l$ . These results imply that fast relaxation timescales are governed by the local plasticity of the contact networks through the particle-scale parameters, such as surface roughness, rigidity, and adhesion. On the other hand, slow timescales involving large scale rearrangements in the

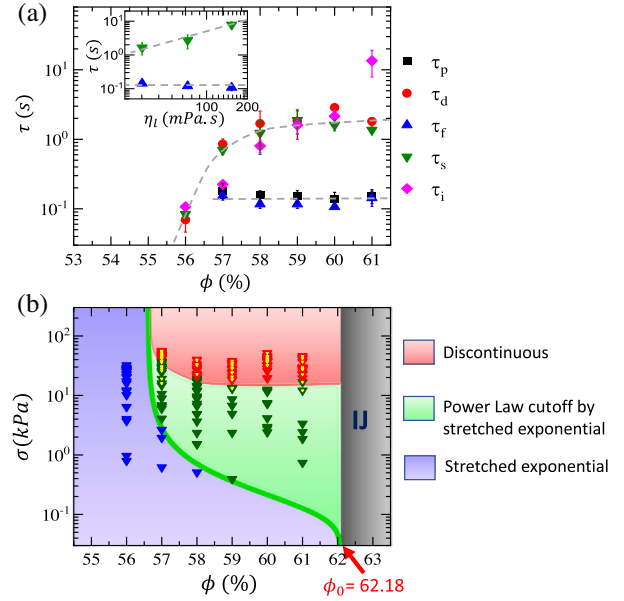


FIG. 3. (a) Dependence of fast ( $\tau_p$  and  $\tau_f$ ) and slow ( $\tau_d$  and  $\tau_s$ ) timescales as a function of volume fraction  $\phi$ .  $\tau_i = 1/\dot{\gamma}_c$  obtained from the steady-state measurements. Inset:  $\tau_f$  and  $\tau_s$  as a function of  $\eta_l$ . Error bars indicate standard deviation over three independent measurements. Gray dashed lines are guides to the eye. (b) State diagram in  $\sigma$ - $\phi$  parameter plane. Thick green line indicates SSSJ onset. In the pink shaded region discontinuous stress relaxation (red triangles) and PCs (yellow dots) are observed, whereas, in the green region (with dark-green triangles), a continuous relaxation (power-law cutoff by a stretched exponential) is found. Below the SSSJ regime (purple region with blue triangles) initial power-law relaxation behavior disappears. Gray shaded region indicates isotropic jamming. In all cases symbols are the peak stress  $\sigma_p$  obtained from the transient relaxation experiments.

system should increase due to the increase in drag (due to the increase in  $\eta_l$ ) or increase in the average coordination number (due to the increase in  $\phi$ ). Such behavior of longer timescales is also observed in simulation [24]. We find that the timescale obtained from the inverse of onset shear rate for shear-thickening under steady shear ( $\tau_i = 1/\dot{\gamma}_c$ ) shows a good agreement with the slow timescales [Fig. 3(a)], similar to flow cessation experiments [23]. These observations further confirm our conjecture about the origin of fast and slow timescales.

Finally, we construct a state diagram summarizing the results of transient stress relaxation in the  $\sigma$ - $\phi$  parameter plane [Fig. 3(b)]. The onset of SSSJ is obtained from the steady-state flow curves (Fig. S1 in the Supplemental Material [31]). As indicated in the diagram, sharp discontinuous stress relaxation (red region) over a short time in the SJ regime is observed for high peak stress values  $\sigma_p > 16$  kPa. PCs also appear in this regime showing a strong correlation with the discontinuous stress relaxation. The capillary stresses at the solvent-air interface provide

the confining stress over a wide range during shear-induced dilation in dense suspensions [4,39,48]. Since PC indicates abrupt local curvature due to significant protrusion of isolated particles or small clusters, the local confining stress at the PC can be approximated as the maximum capillary stress  $\sim \Gamma/a \approx 16$  kPa. Such capillary stress drives the protruding particle inside the bulk during the discontinuous stress relaxation over a timescale  $\eta_t a/\Gamma \sim 0.1$  s ( $\eta_t = \sigma_p/\dot{\gamma}_p$ ; see the Supplemental Material [31] for text and Fig. S10). This timescale is close to the fast relaxation timescale observed in our system. Intriguingly, in between the discontinuous stress relaxation regime and onset of SSSJ (green region), we obtain a smooth relaxation regime [Fig. 3(b)] where  $\sigma(t) \sim t^{-\alpha} e^{-(t/\tau)^\beta}$ . Below SSSJ, the initial power-law relaxation regime disappears.

In conclusion, we identify two distinct transient stress relaxation regimes in SJ dense suspensions originating from the dynamics of localized plasticity and system spanning dilation. Recently, intrinsic contact-relaxation timescales have been extracted from the coupling of relaxation with the instrument inertia [43]. Also, considering plasticity in the system, recent theoretical models [24] capture the short-time stress relaxation behavior. Although the relaxation timescales in our system are within the range predicted in Ref. [43], the robust initial power-law decay, presumably coming from stress induced force chain buckling or breaking cannot be predicted from these models. We find that the fast and slow relaxation timescales are almost independent of step-strain magnitude (Fig. S11 in the Supplemental Material [31]) and the estimated diffusion timescales are inadequate to quantitatively capture them (Supplemental Material [31]). Our preliminary data for larger polystyrene particles (mean diameter:  $6.5 \mu\text{m}$ ) also show similar relaxation dynamics. However, these directions including a possible extension into the Brownian regime, require further exploration using more sophisticated experimental techniques [49]. We find an interesting correlation between the transient stress relaxation and the steady-state shear jamming. The continuous stress relaxation showing a power-law cutoff by stretched-exponential behavior is reminiscent of relaxation in frictionless systems close to jamming implying that for well-constrained systems the relaxation dynamics is not sensitive to the exact origin of the constraints. Such functional form indicates a wide range of underlying relaxation modes in the system [50]. We also observe similar relaxation behavior including the discontinuous stress relaxation for other SJ dense suspensions, indicating an universal behavior. Although our study underscores the importance of local plasticity in controlling the mechanical behavior of SJ systems, deciphering the microscopic nature and dynamics of such plasticity, together with a possible connection to the more general framework of soft glassy rheology [26,27,46,51] potentially unifying the relaxation behaviour in SJ and glassy systems, remains an important future direction.

S. M. thanks SERB (under DST, Govt. of India) for support through a Ramanujan Fellowship (Award reference No. SB/S2/RJN-123/2017). We thank Sidney Nagel for helpful discussions and K. M. Yatheendran for help with SEM imaging.

\*smajumdar@rri.res.in

- [1] H. Barnes, *J. Rheol.* **33**, 329 (1989).
- [2] R. Hoffman, *Trans. Soc. Rheol.* **16**, 155 (1972).
- [3] N. J. Wagner and J. F. Brady, *Phys. Today* **62**, No. 10, 27 (2009).
- [4] E. Brown and H. M. Jaeger, *Rep. Prog. Phys.* **77**, 046602 (2014).
- [5] E. Brown, N. A. Forman, C. S. Orellana, H. Zhang, B. W. Maynor, D. E. Betts, J. M. DeSimone, and H. M. Jaeger, *Nat. Mater.* **9**, 220 (2010).
- [6] M. Wyart and M. E. Cates, *Phys. Rev. Lett.* **112**, 098302 (2014).
- [7] R. Seto, R. Mari, J. F. Morris, and M. M. Denn, *Phys. Rev. Lett.* **111**, 218301 (2013).
- [8] R. Mari, R. Seto, J. F. Morris, and M. M. Denn, *J. Rheol.* **58**, 1693 (2014).
- [9] B. M. Guy, M. Hermes, and W. C. K. Poon, *Phys. Rev. Lett.* **115**, 088304 (2015).
- [10] Y. S. Lee, E. D. Wetzel, and N. J. Wagner, *J. Mater. Sci.* **38**, 2825 (2003).
- [11] A. Majumdar, B. S. Butola, and A. Srivastava, *Mater. Des.* **46**, 191 (2013).
- [12] I. R. Peters, S. Majumdar, and H. M. Jaeger, *Nature (London)* **532**, 214 (2016).
- [13] S. Majumdar, I. R. Peters, E. Han, and H. M. Jaeger, *Phys. Rev. E* **95**, 012603 (2017).
- [14] E. Han, I. R. Peters, and H. M. Jaeger, *Nat. Commun.* **7**, 1 (2016).
- [15] A. Singh, S. Pednekar, J. Chun, M. M. Denn, and J. F. Morris, *Phys. Rev. Lett.* **122**, 098004 (2019).
- [16] B. M. Guy, J. A. Richards, D. J. M. Hodgson, E. Blanco, and W. C. K. Poon, *Phys. Rev. Lett.* **121**, 128001 (2018).
- [17] N. M. James, E. Han, R. A. L. de la Cruz, J. Jureller, and H. M. Jaeger, *Nat. Mater.* **17**, 965 (2018).
- [18] S. Dhar, S. Chattopadhyay, and S. Majumdar, *J. Phys. Condens. Matter* **32**, 124002 (2020).
- [19] A. Singh, C. Ness, R. Seto, J. J. de Pablo, and H. M. Jaeger, *Phys. Rev. Lett.* **124**, 248005 (2020).
- [20] S. Jamali and J. F. Brady, *Phys. Rev. Lett.* **123**, 138002 (2019).
- [21] A. S. Baumgarten and K. Kamrin, *Proc. Natl. Acad. Sci. U.S.A.* **116**, 20828 (2019).
- [22] P. d'Haene, J. Mewis, and G. Fuller, *J. Colloid Interface Sci.* **156**, 350 (1993).
- [23] R. Maharjan and E. Brown, *Phys. Rev. Fluids* **2**, 123301 (2017).
- [24] A. S. Baumgarten and K. Kamrin, *J. Rheol.* **64**, 367 (2020).
- [25] S. Cao, Q. He, H. Pang, K. Chen, W. Jiang, and X. Gong, *Smart Mater. Struct.* **27**, 085013 (2018).
- [26] L. Mohan, M. Cloitre, and R. T. Bonnecaze, *J. Rheol.* **59**, 63 (2015).

- [27] Y. Chen, S. A. Rogers, S. Narayanan, J. L. Harden, and R. L. Leheny, *Phys. Rev. Mater.* **4**, 035602 (2020).
- [28] S. R. Waitukaitis and H. M. Jaeger, *Nature (London)* **487**, 205 (2012).
- [29] T. Hatano, *Phys. Rev. E* **79**, 050301(R) (2009).
- [30] A. Ikeda, T. Kawasaki, L. Berthier, K. Saitoh, and T. Hatano, *Phys. Rev. Lett.* **124**, 058001 (2020).
- [31] See Supplemental Material at <http://link.aps.org/supplemental/10.1103/PhysRevLett.128.258002> for additional experimental details, results and analysis.
- [32] D. Wang, B. Yu, H.-L. Cong, Y.-Z. Wang, Q. Wu, and J.-L. Wang, *Integr. Ferroelectr.* **147**, 41 (2013).
- [33] A. Singh, R. Mari, M. M. Denn, and J. F. Morris, *J. Rheol.* **62**, 457 (2018).
- [34] <https://omnexus.specialchem.com/polymer-properties/properties/young-modulus> (2022).
- [35] B. Utter and R. P. Behringer, *Phys. Rev. E* **69**, 031308 (2004).
- [36] R. Besseling, E. R. Weeks, A. B. Schofield, and W. C. K. Poon, *Phys. Rev. Lett.* **99**, 028301 (2007).
- [37] P. Olsson, *Phys. Rev. E* **81**, 040301(R) (2010).
- [38] C. Eisenmann, C. Kim, J. Mattsson, and D. A. Weitz, *Phys. Rev. Lett.* **104**, 035502 (2010).
- [39] E. Brown and H. M. Jaeger, *J. Rheol.* **56**, 875 (2012).
- [40] J. R. Royer, D. L. Blair, and S. D. Hudson, *Phys. Rev. Lett.* **116**, 188301 (2016).
- [41] S. Bakshi, V. V. Mohanan, R. Sarkar, and S. Majumdar, *Soft Matter* **17**, 6435 (2021).
- [42] R. Seto, A. Singh, B. Chakraborty, M. M. Denn, and J. F. Morris, *Granular Matter* **21**, 82 (2019).
- [43] J. A. Richards, J. R. Royer, B. Liebchen, B. M. Guy, and W. C. K. Poon, *Phys. Rev. Lett.* **123**, 038004 (2019).
- [44] M. E. Cates, J. Wittmer, J.-P. Bouchaud, and P. Claudin, *Phys. Rev. Lett.* **81**, 1841 (1998).
- [45] A. Amon, V. B. Nguyen, A. Bruand, J. Crassous, and E. Clément, *Phys. Rev. Lett.* **108**, 135502 (2012).
- [46] A. Le Bouil, A. Amon, S. McNamara, and J. Crassous, *Phys. Rev. Lett.* **112**, 246001 (2014).
- [47] Y. Cao, J. Li, B. Kou, C. Xia, Z. Li, R. Chen, H. Xie, T. Xiao, W. Kob, L. Hong *et al.*, *Nat. Commun.* **9**, 1 (2018).
- [48] L. A. Slobozhanin, J. I. D. Alexander, S. H. Collicott, and S. R. Gonzalez, *Phys. Fluids* **18**, 082104 (2006).
- [49] S. Pradeep, M. Nabizadeh, A. R. Jacob, S. Jamali, and L. C. Hsiao, *Phys. Rev. Lett.* **127**, 158002 (2021).
- [50] D. Hexner, A. J. Liu, and S. R. Nagel, *Soft Matter* **14**, 312 (2018).
- [51] P. Sollich, F. Lequeux, P. Hébraud, and M. E. Cates, *Phys. Rev. Lett.* **78**, 2020 (1997).